





Helium plumes at moderate Reynolds number

Stefano Lanzini ^{*}, Massimo Marro , and Mathieu Creyssels 
*Ecole Centrale de Lyon, CNRS, Universite Claude Bernard Lyon 1, INSA Lyon,
LMFA, UMR5509, 69130 Ecully, France*

Pietro Salizzoni 
*Ecole Centrale de Lyon, CNRS, Universite Claude Bernard Lyon 1, INSA Lyon,
LMFA, UMR5509, 69130 Ecully, France*
*and Department of Environmental, Land and Infrastructure Engineering (DIATI), Politecnico di Torino,
Corso Duca degli Abruzzi 24, 10129 Turin, Italy*



(Received 5 October 2023; accepted 1 May 2024; published 11 June 2024)

We present an experimental investigation of the turbulent entrainment in non-Boussinesq steady plumes, focusing on three helium releases issued from an axisymmetric source, and with increasing Reynolds number. Two-dimensional instantaneous velocity fields, measured using particle image velocimetry (PIV), are exploited to compute first- and second-order velocity statistics focusing on the near field, i.e., up to a distance of a few tens of source radii. Flow visualizations and velocity statistics profiles are investigated to describe the flow transition from a quasilaminar zone, governed by Rayleigh-Taylor instability, to a more distinctly turbulent region. The vertical evolution of the integral fluxes, the Richardson number, and the entrainment coefficient are presented enlightening the influence of an increasing Reynolds number at the source. The plume characteristic density is reconstructed based on the assumption, sustained by recent literature data, of a null-divergence flow. Making use of the entrainment decomposition, we investigate the contribution of the different physical mechanisms involved in the mixing process at varying distances from the source, with a focus on the effect of the local density ratio. Our results show that the variations of the entrainment coefficient in the turbulent region are primarily affected by the near-field generation of turbulent kinetic energy and by a rising contribution of buoyancy effects. Both features do not exhibit a clear dependence on local variations of the density ratio.

DOI: [10.1103/PhysRevFluids.9.064501](https://doi.org/10.1103/PhysRevFluids.9.064501)

I. INTRODUCTION

Plumes are vertical flows that arise from a localized source of buoyancy. They are a widely investigated topic in fluid mechanics because of their presence in several areas of engineering and physical sciences, e.g., ocean outfalls, exhausts of engines, volcanic eruptions, and fire-induced smoke. A robust approach in the modeling of plumes generated by a circular source is provided by the “plume equations” [1], i.e., an integral description of the flow, in which spatially averaged variables depend only on the distance from the source, z . In this framework, the key parameter is the so-called entrainment coefficient, α , which controls the dilution of the plume with the ambient fluid. Morton *et al.* [1], and most of the subsequent theoretical and experimental studies on this topic (the main results are resumed in the review papers of List [2], Kaye [3], and Woods [4]), deal with

^{*}Corresponding author: stefano.lanzini@doctorant.ec-lyon.fr

the so-called ‘‘Boussinesq plumes,’’ characterized by slight (i.e., less than 10%) density differences between the plume and the surrounding fluid. In this framework, assuming a fully turbulent plume developing in a nonstratified quiescent environment and neglecting molecular diffusion, the flow dynamics can be shown [5] to depend on a single nondimensional parameter, the scaled plume Richardson number, defined as [6]

$$\Gamma(z) = \frac{5}{8\alpha_p} \text{Ri}(z) = \frac{\text{Ri}(z)}{\text{Ri}_p}, \quad (1)$$

where $\alpha_p = 0.12$ is a reference far-field value for the pure plumes entrainment coefficient, obtained considering top-hat profiles [1,7,8], and the Richardson number, representative of the ratio of buoyant to inertial forcing, is defined as $\text{Ri} = g(\rho_0 - \rho_m)r_m/\rho_0 w_m^2$, where g is the gravitational acceleration, ρ_0 is the ambient density, and ρ_m , r_m , and w_m are the local characteristic density, radius, and velocity, respectively (see Sec. IV for precise definitions). The so-called ‘‘pure plume’’ equilibrium condition, with $\text{Ri}_p = 8\alpha_p/5$, is reached in the far field of any turbulent buoyant release, independently of its condition at the source [6]. By construction, $\Gamma = 1$ for a pure plume. This condition sets a distinction between forced plumes, which have an excess of momentum (relative to pure plume conditions), $0 < \Gamma < 1$, and lazy plumes, which have a deficit of momentum ($\Gamma > 1$).

The body of literature that deals with releases characterized by large density differences at the source, i.e., the ‘‘non-Boussinesq’’ releases, is significantly smaller. In the early work of Batchelor [9], a reduced turbulent mixing was observed, with respect to the Boussinesq case, in starting plumes significantly lighter than the ambient fluid. In the following decades, the only experimental study that sought to elucidate the effects of large density differences on the entrainment coefficient was the work of Ricou and Spalding [10]. Based on experiments on variable-density jets (i.e., $\Gamma = 0$), they inferred that the entrainment is increased for an increasing ratio between the local characteristic density and the ambient density, following the powerlaw

$$\alpha = \alpha_0 \left(\frac{\rho_m}{\rho_0} \right)^{1/2}, \quad (2)$$

where $\alpha_0 = \alpha_j$ is the entrainment coefficient in the far field of the jet (where the effects of density differences between the release and the ambient are lost). This result has created the basis for subsequent works (e.g., [11–14]) in which Eq. (2) is assumed to be valid (in the absence of any further experimental confirmation) even for non-Boussinesq plumes, simply by considering $\alpha_0 = \alpha_p$. However, the adoption of Eq. (2) for non-Boussinesq plumes raises several issues. Firstly, recent experiments and simulations of Salizzoni *et al.* [15] on variable-density jets do not support the scaling proposed by Ricou and Spalding [10]. Secondly, its extension to non-Boussinesq plumes is not based on any robust experimental evidence. Moreover, the relation (2) suggests an entrainment phenomenology relative to the density differences that is somehow controversial. According to well-established literature on buoyant jets and plumes [5,6,8,16–18], a reduced density of the release would imply a larger Γ , resulting in an enhanced entrainment coefficient. For $0 < \Gamma < 1$, this feature is outlined by the following relation for α [6,16,17]:

$$\alpha = \alpha_j + \Gamma(\alpha_p - \alpha_j), \quad (3)$$

where $\alpha_p > \alpha_j$. According to Eq. (2), the entrainment coefficient would instead be reduced by a smaller plume density, and its dependence on the local Γ neglected.

The limited understanding of the role of density ratio in the entrainment process derives essentially from a lack of experimental studies on non-Boussinesq plumes. These releases have rarely been investigated experimentally because of the complexity of their reproduction at laboratory scale. High-density differences plumes are typically generated by fires [19,20] or by very light gases that must be properly stocked. The technical hurdle relies on obtaining a sufficiently high buoyant forcing (compared to the inertial one) such that $\Gamma \geq 1$, while maintaining a sufficiently high Reynolds number at the source. Most experimental studies on non-Boussinesq releases focus

on flows where the required buoyant forcing is smaller, such as turbulent jets [10,15,21] or forced plumes [22,23]. Given the ease of its stocking, its low cost, and its low density, the most convenient gas that is fit to recreate, in the laboratory, a release with a low-density ratio, is helium. The ratio of the kinematic viscosities of helium and air at ambient temperature at atmospheric pressure is 7.7 [24,25]. The Reynolds number of a helium release is reduced by a factor of 7.7 compared to a pure air release. Therefore, to recreate a high-Reynolds, laboratory plume that is simultaneously non-Boussinesq and with Γ close to unity, it is necessary to increase its spatial scale. For example, a helium lazy plume issued by a 1-m-diameter source was reproduced by O’Hern *et al.* [26] but the measurements were performed only up to a maximum of 1 diameter in height.

Given these controversial aspects, this work aims at providing a step forward in the understanding of the density ratio role in the mixing process and presents an experimental investigation of the entrainment in non-Boussinesq steady plumes. We focus on three helium plumes with increasing Reynolds numbers at the source, Re_s , defined as $\text{Re}_s = 2w_s r_s / \nu_s$, where r_s is the source radius and w_s and ν_s are the mean vertical velocity and kinematic viscosity at the injection, respectively. In this framework, considering a nonreacting plume in a nonstratified environment, the entrainment coefficient α is expected to depend on the following nondimensional quantities:

$$\alpha = \alpha \left(\Gamma_s, \frac{\rho_s}{\rho_0}, \text{Re}_s, \text{Sc}_s, \frac{\nu_s}{\nu_0}, \frac{z}{r_s} \right), \quad (4)$$

where the subscript “s” refers to the value of the quantity at the source. The Schmidt number at the source, $\text{Sc}_s = \nu_s / D$, equal to the ratio between the kinematic viscosity at the source ν_s and the species diffusivity D , and the ratio between the kinematic viscosity at the source and the ambient one, ν_0 , will be fixed for all the experiments and their influence on the entrainment phenomenon will not be explored in the following. The explicit dependence on the distance from the source, z/r_s , can be made implicit by considering the dimensionless parameters defined locally (i.e., for a given distance from the source [15]). Therefore, we will investigate the following relation:

$$\alpha = \alpha \left(\Gamma, \frac{\rho_m}{\rho_0}, \text{Re}_m \right), \quad (5)$$

where $\text{Re}_m = 2r_m w_m / \nu_m$ is the local Reynolds number, based on the local characteristic radius, velocity, and viscosity (see Sec. IV for the definition of the characteristic quantities).

A full characterization of non-Boussinesq plume statistics would require simultaneous measurement of velocity and density. However, the works of Salizzoni *et al.* [15] on variable-density jets and O’Hern *et al.* [26] on the near-source region of non-Boussinesq lazy plumes have shown that the Reynolds and Favre first- and second-order statistics are almost coincident. In the remainder of the paper, we will assume that this holds also for non-Boussinesq pure plumes: all subsequent analysis will therefore rely on Reynolds-averaged statistics only. This allows us to significantly simplify the experimental setup, performing only velocity measurements obtained by the PIV technique. The experimental details are presented in Sec. II. A description of the flow is presented in Sec. III, relying on flow visualizations and on the presentation of first- and second-order velocity statistics profiles. The analysis of the integral flow dynamics is shown in Sec. IV and it is performed by evaluating the plume fluxes, the characteristic quantities, and Γ at different heights from the source. The computation of the entrainment coefficient is performed in two ways. The first is based on the radial integration of the volume conservation equation closed with the classical entrainment hypothesis [27]. The second relies on the entrainment decomposition [6,16,28], obtained by manipulating the mean-kinetic energy and the momentum equations. This relation was deployed both experimentally and numerically in recent works on jets and Boussinesq plumes [5,15,18,29], fountains [30,31], and gravity currents [32] but so far never exploited for non-Boussinesq plumes. The dependence of the entrainment coefficient and of the entrainment decomposition terms on the local density ratio and local Richardson and Reynolds numbers is discussed in Sec. V. Conclusions are reported in Sec. VI.

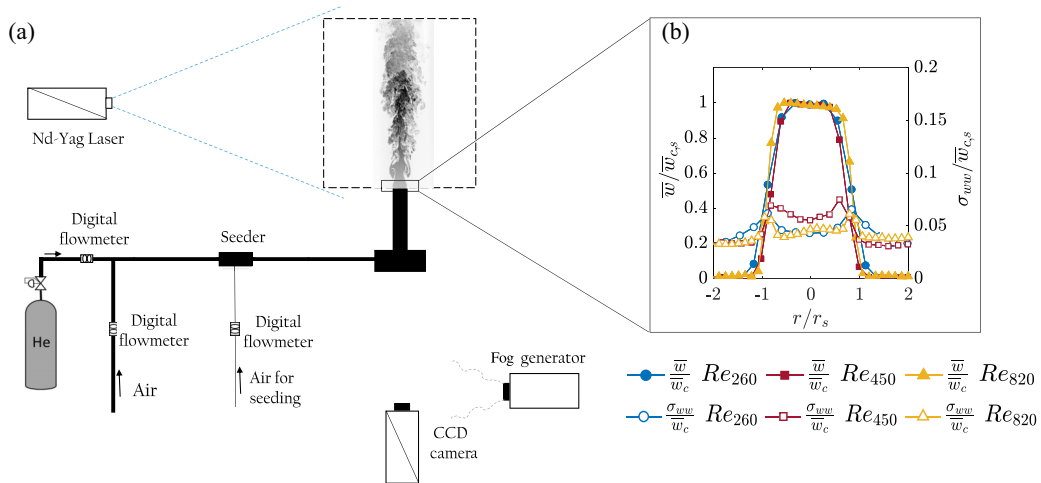


FIG. 1. (a) Sketch of the experimental setup. (b) Radial profiles at the source of the mean vertical velocity, \overline{w} , and the rms of vertical velocity fluctuations, σ_{ww} . All the profiles are normalized with the source mean centerline velocity, $\overline{w}_{c,s}$.

II. EXPERIMENTAL SETUP

The experiments aim at establishing first- and second-order velocity statistics in a plane of non-Boussinesq plumes with varying Reynolds number at the source. The measurement technique is a two-dimensional PIV, obtained on a single measurement window, placed just above the plume source. The plumes are generated using a helium–air gas mixture supplied through a 70-cm-long vertical pipe. The gas mixture has a density ratio ρ_s/ρ_{amb} at the source equal to 0.2. The volume fluxes of helium and air are provided by two flow controllers. The helium molar fraction, needed to impose this density ratio at the source, is 0.93. In order to have a homogeneous flow, the mixing between air and helium takes place far upstream of the entrance to the source pipe [see Fig. 1(a) for a sketch of the experimental setup]. Three different plumes with Reynolds numbers at the source equal to 260, 450, and 820 are studied, referred to hereafter as Re_{260} , Re_{450} , and Re_{820} . All three plumes have $\Gamma = 1$ at the source and the same density ratio, ρ_s/ρ_{amb} . In order to keep these two parameters constant and to change only the Reynolds number, both the volume flow rate and the exit area of the source are changed in the three experiments. The exit radial profiles of the mean vertical velocity, \overline{w} , and of the rms of vertical velocity fluctuation, σ_{ww} , scaled with the mean source centerline velocity, $\overline{w}_{c,s}$, are shown in Fig. 1(b). The source conditions are summarized in Table I. For the three experimental plumes, the source Schmidt number is 1.69 and the viscosity ratio is 7.1.

A. PIV acquisition parameters

A dual-head Nd:yttrium aluminum garnet laser (Litron Bernoulli-PIV 200-15) and a 12-bit CCD camera with 3280×4920 pixel resolution are synchronized so that a close pair of laser pulses

TABLE I. Experimental source conditions.

	Re_{260}	Re_{450}	Re_{820}
Γ	1	1	1
Source diameter d_s (cm)	3.5	5	7.5
Exit velocity w_s (m/s)	0.82	0.98	1.20
ρ_s/ρ_{amb}	0.2	0.2	0.2
Volume flux at the source πQ_s (m^3/s)	7.9×10^{-4}	1.92×10^{-3}	5.31×10^{-3}

corresponds to a close pair of camera shots. The pulses produce a laser sheet that passes through a plume symmetry plane that is perpendicular to the camera's optical axis, and the light reflected by the seeding particles is captured by the camera. The commercial PIV system LaVision DaVis is used for acquisition. The cross-correlation is performed on areas of 64×64 pixels and exploits a 50% overlap between the areas, and a 103×154 element velocity vector field is obtained. The size of the image is $52.5 \text{ cm} \times 78.5 \text{ cm}$, with a spatial resolution of 5.1 mm. Since the source exit radius r_s is different for the three plumes, the maximum measurement height (expressed in terms of source radii) changes between the experiments. These are $44.6r_s$, $31.2r_s$, and $20.8r_s$ for Re_{260} , Re_{450} , and Re_{820} , respectively.

PIV measurements require seeding both the mixture exiting from the source (internal seeding) and the ambient air (external seeding). The internal seeding is obtained with micronic oil droplets and the external one is obtained with a fog generator emitting droplets in the range $0.5\text{--}2 \mu\text{m}$. After generating the external seeding, we waited several minutes to allow the particles to achieve a uniform distribution in the room and for ambient velocity fluctuations to attenuate. It is worth checking that the PIV image brightness induced by internal seeding is equal to the brightness induced by external seeding. After every modification in the position of the camera or in the position of the laser head, the LaVision PIV system was recalibrated (using a calibration grid). The software receives as input the geometrical measure of the grid dots, the global dimension of the calibration panel, the position of the center of the grid, and self-calibrates to obtain proper velocity measurements.

Since the exit velocity changes between the three plumes, different Δt between the impulses are used for the three source conditions, in order to guarantee the accuracy of the results. For each plume, 1500 instantaneous velocity fields are acquired with a frequency of 3.3 Hz, allowing the first and second-order velocity statistics to be computed accurately [33].

B. Measurements uncertainties

Following recent studies [15,34,35], we consider that, at first order, the most relevant source of the experimental errors is the precision uncertainty due to the finite number of samples. This is locally estimated, for mean vertical velocity, $\overline{w}(r, z)$, and for the axial-normal and shear components of the Reynolds stress tensor, $\overline{w'w'}(r, z)$ and $\overline{w'u'}(r, z)$, following the method presented in Benedict and Gould [36], considering a 95% confidence interval. For \overline{w} , the experimental errors along the centerline do not exceed 2%, while they are close to 6% at the edges of the plume. In this region, also the errors on $\overline{w'w'}$ have a maximum, while, for smaller radial distances, they do not exceed 8%. The errors on Reynolds shear stress $\overline{w'u'}$, instead, have a maximum in the proximity of the centerline, where the absolute value of $\overline{w'u'}$ is close to zero. In the rest of the domain, they are approximately 12%.

The propagation of the errors on the velocity statistics is employed to estimate errors on all quantities in Sec. IV, where all the plots are presented with error bars (when these are not present their amplitude is below 5%). To that purpose, we generate, for each velocity statistic, 100 fictitious fields, whose local values are given by the sum of the measured value of the reference statistic and of a zero-mean Gaussian random variable. The standard deviation of the random variable is half of the precision uncertainty. This process allows evaluating 100 vertical profiles for each quantity of Sec. IV. The vertical profiles and error bars correspond to the local mean value and to the width of the 95% confidence interval obtained from the 100 vertical profiles, respectively.

III. FLOW DESCRIPTION

A. Flow visualization

The starting point of our analysis is a phenomenological description of the flow, considering the instantaneous visualizations of Fig. 2. The flow visualizations can be easily obtained from the set up described in Sec II, removing the seeding of the ambient air. For the three Re_s , it is possible

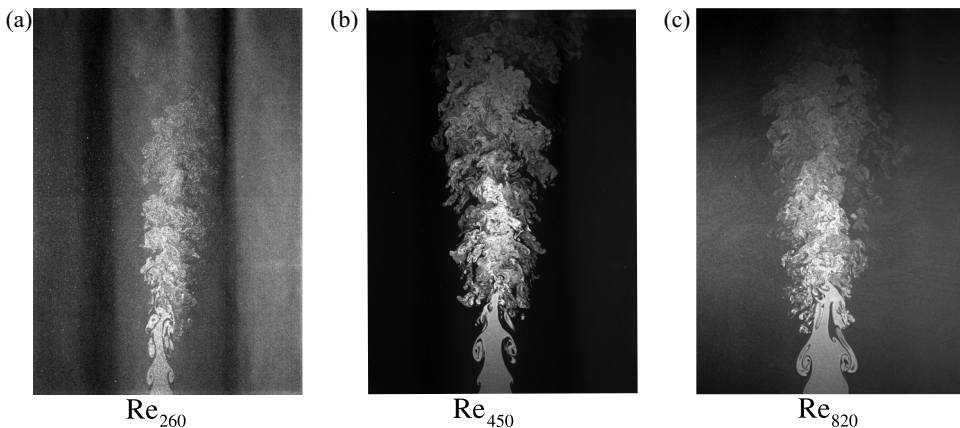


FIG. 2. Instantaneous visualization of the three experimental plumes.

to distinguish two distinct regimes in the observed domain, identified by different flow kinematics. In the near-source region, the plumes are governed by a local absolute instability dynamics [37], characterized by the formation of large vortex rings that govern the flow without triggering an evident energy transfer to smaller-scale structures. These toroidal structures, which are typically the signature of a Rayleigh-Taylor instability, have been observed in the near-source region of jets [38,39] and plumes [25,40–42]. Their dynamics is related to a characteristic “puffing” frequency, which exhibits a clear dependence on both the Reynolds and the Richardson numbers [25]. From Fig. 2, it is evident that, for Re_{260} , a larger number of vortex rings is present simultaneously in the streamwise direction with respect to the cases with higher Re_s . For the three experiments, the processes involved in the growth, interaction, and breakdown of vortices evolve temporally in a periodic way. The breaking of the organized structures and the subsequent destruction of the potential core results in the formation of small-scale eddies, giving rise to typical features characterizing a turbulent flow regime.

B. Local flow statistics

The second step in our analysis is a detailed description of first- and second-order velocity statistics. The aims of this analysis, other than widening the so-far limited literature on the experimental data on non-Boussinesq plumes, are to evaluate (i) the signature of the two differing flow regimes in the statistical flow response and (ii) the dependency on Re_s of the velocity statistics. To have a general overview of the flow and exploiting axial symmetry, the nondimensional mean vertical velocity, \bar{w}/w_s , Reynolds shear stresses, $\overline{w'u'}/w_s^2$, and turbulent kinetic energy, k/w_s^2 , are shown in Fig. 3. Assuming isotropy on the horizontal plane [18,43], the latter is estimated as $k \simeq 1/2(\overline{w'w'} + \overline{u'u'})$, where $\overline{w'w'}$ and $\overline{u'u'}$ are the axial-normal and radial-normal components of the Reynolds stress tensor.

Both the vertical and the radial distances are scaled with the source radius, r_s . In order to have a direct comparison between the different plumes, in the remainder of the paper, the results for the three experiments will be presented up to a maximum height of 20 source radii (the upper limit of the measurement domain for Re_{820}). Variations in the Reynolds number at the source show little influence on the first-order statistics (\bar{w}) [Figs. 3(a)–3(c)] but become evident when considering second-order statistics. The turbulent kinetic energy fields [Figs. 3(g)–3(i)] show a peak that approaches the source for increasing Re_s , revealing the faster triggering of turbulence within the potential core as the Reynolds number increases. This behavior is consistent with the visualizations in Fig. 2: for Re_{260} , multiple vortex rings are simultaneously present in the streamwise direction.

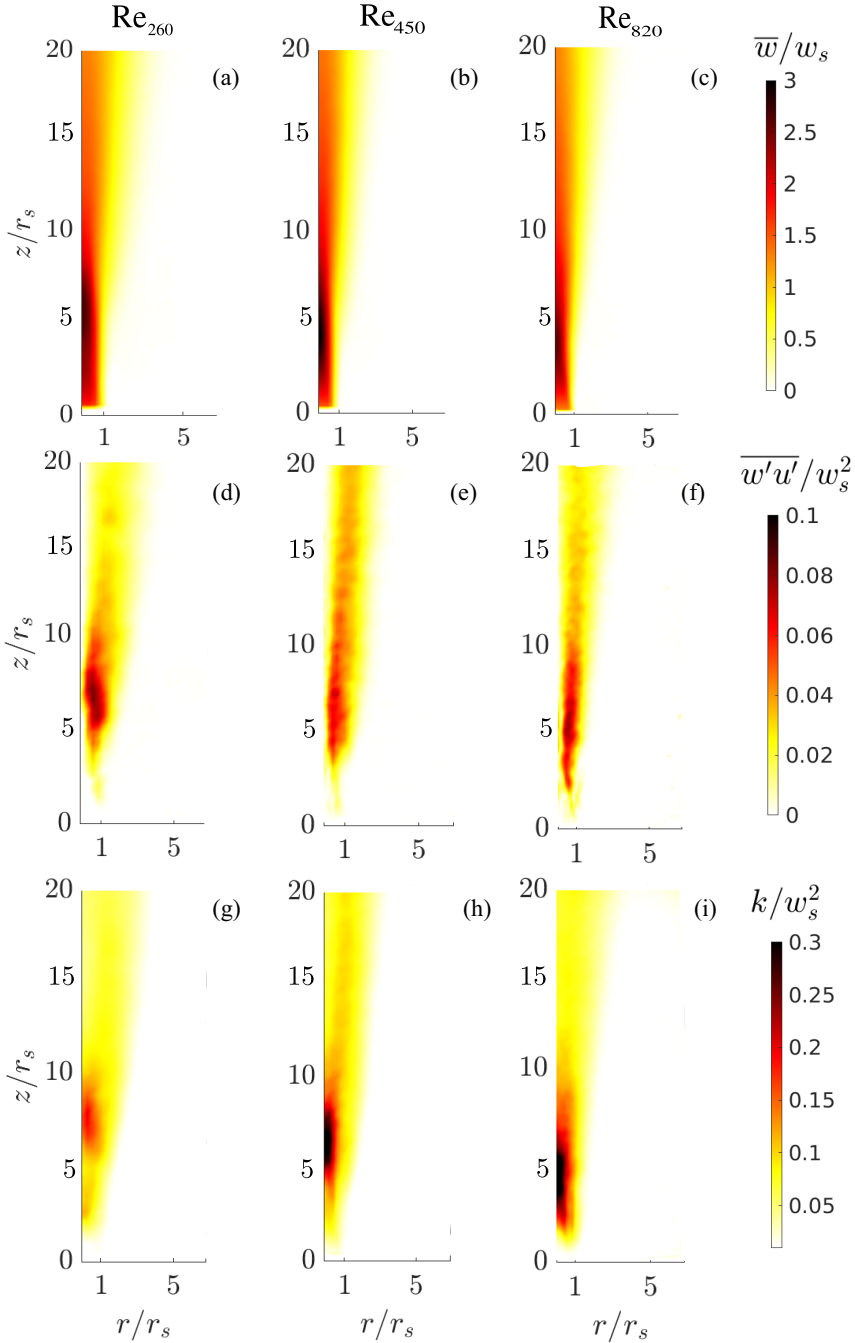


FIG. 3. First- and second-order statistics fields for the three experimental plumes: (a)–(c) show the mean vertical velocity fields \bar{w} scaled with the vertical velocity at the source w_s ; (d)–(f) show the shear Reynolds stress fields $\overline{w'u'}$ scaled with w_s^2 ; and (g)–(i) are the turbulent kinetic energy fields k scaled with w_s^2 . Both the vertical and the radial positions are scaled with the source radius r_s .

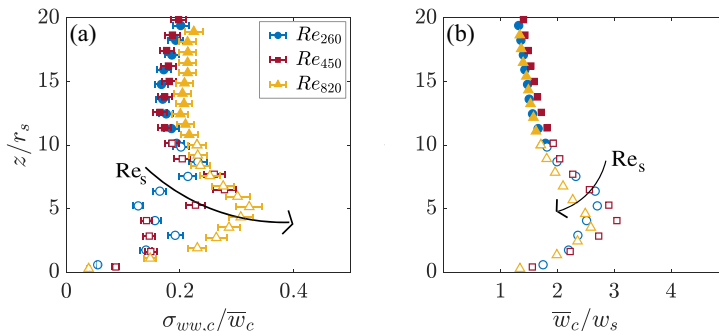


FIG. 4. Evolution of the rms vertical velocity fluctuation, $\sigma_{ww,c}$ (a), and of the mean centerline vertical velocity, \bar{w}_c (b), for the three experimental plumes. Hollow and filled markers refer to the quasilaminar and turbulent zones, respectively.

This implies a larger extension of the region dominated by the Rayleigh-Taylor instability, compared to cases with higher Re_s .

The effect of the turbulent transition is evident also on the axial profiles of the rms vertical velocity fluctuations $\sigma_{ww,c}$, shown in Fig. 4(a). For the three experiments, $\sigma_{ww,c}$ is null at the source, it increases for $0 < z/r_s < 6r_s$, reaches a maximum, and decreases. Increasing the Reynolds number, the vertical distance from the source of the peak diminishes, and the maximum value increases. In addition, we observe a varying shape of the axial profile: for Re_{820} , the growth until the peak is monotonic, for Re_{450} , there is an inflection point below the peak, at $z = 3r_s$, and for Re_{260} , there is a relative maximum at the same position. Similar overshoot in the $\sigma_{ww,c}$ vertical profile has been already observed for variable-density transitional jets by Kyle and Sreenivasan [38] and Viggiano *et al.* [21]. Relying on spectral analysis, Kyle and Sreenivasan [38] have shown that the overshoot in $\sigma_{ww,c}$ is primarily associated with the vortices pairing process. This may account for the observed double peak in Re_{260} , as an increased number of vortices can lead to a higher number of interactions among them, resulting in multiple peaks of $\sigma_{ww,c}$. For $z > 10r_s$, downstream of the structure breakdown and of the pinch off of the potential core (i.e., where the turbulent regime is established), there are no longer abrupt variations in $\sigma_{ww,c}$. The distinction between the region identified by organized structures and the one characterized by a disorganized state related to classical turbulence will be maintained also in Sec. IV and will be highlighted by the use of hollow and filled markers, respectively. The $z > 10r_s$ zone will be referred to as “turbulent region” in the following. The axial profiles of vertical centerline velocity \bar{w}_c , shown in Fig. 4(b), confirm that, for first-order statistics, the Reynolds dependence is less evident. Our moderate-Reynolds, non-Boussinesq pure plumes show a \bar{w}_c acceleration above the source, up to $3w_s$, and then a deceleration.

Other relevant features of the flow concern the evolution of the Reynolds stress tensor components at various distances from the source, shown in Fig. 5, where all the profiles are scaled with the mean centerline vertical velocity squared and the radial distance with z . The profiles are compared with the fully self-similar radial profiles provided by Wang and Law [8] (hereon referred to as W&L), measured in the far field ($z > 100r_s$) of a pure plume. For the $\overline{w'u'}$ component [Figs. 5(a)–5(c)], the values gradually increase moving downstream from the source and, above $15r_s$, the profiles approach self-similarity. The peak value, equal for the three plumes, $\overline{w'u'}/\bar{w}_c^2 \approx 0.017$, is slightly smaller than the peak registered by W&L, i.e., $\overline{w'u'}/\bar{w}_c^2 \approx 0.021$. The influence of a varying Reynolds number is evident in the radial profiles of axial normal $\overline{w'w'}$ and radial normal $\overline{u'u'}$ stresses [Figs. 5(d)–5(i)]. Near the source, at $z = 5r_s$, the vertical velocity fluctuations are small, compared to the far-field value, for Re_{260} [Fig. 5(d)] and Re_{450} [Fig. 5(e)] but they show a big overshoot in Re_{820} [Fig. 5(f)]. Just downstream, at $z = 8r_s$, the situation is reversed with a sharp increase of $\overline{w'w'}$ in Re_{260} and Re_{450} but a decrease in Re_{820} with respect to the values at $z = 5r_s$.

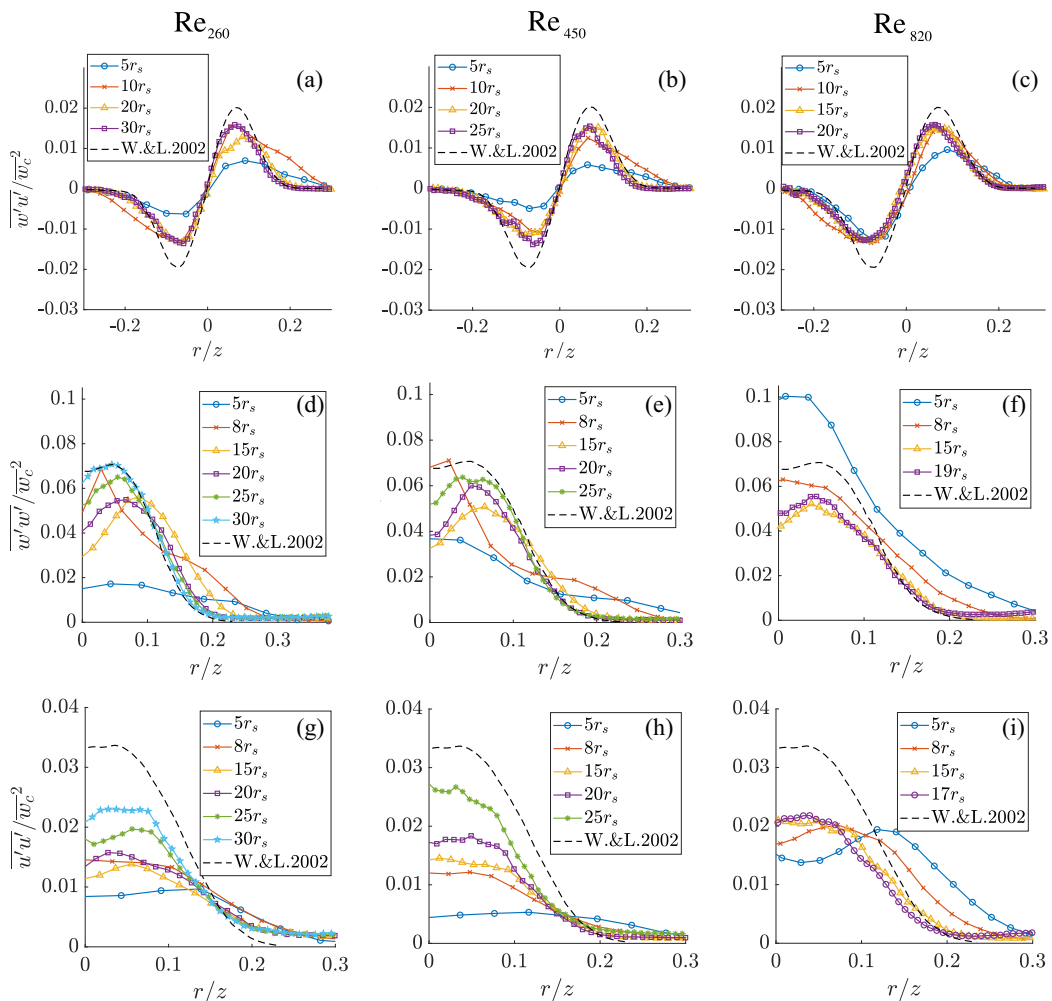


FIG. 5. Radial profile for the three plumes of $\overline{w'u'}$ (a)–(c), $\overline{w'w'}$ (d)–(f), and $\overline{u'u'}$ (g)–(i) obtained at different distances from the source. In order to seek for self-similar behavior, the flow statistics are scaled with $\overline{w_c^2}$ and the radial distance with z . The results are systematically compared with the radial profiles measured by Wang and Law [8] (black dashed line) for a pure plume in full self-similar condition.

This peculiar behavior confirms a faster turbulent triggering for increasing Re_s . Once the peak of fluctuations related to the transition occurs, the profiles gradually approach the W&L reference values. The effects of turbulent transition are less evident in the case of radial normal stresses $\overline{u'u'}$ [Figs. 5(g)–5(i)], despite the occurrence of an overshoot at $5r_s$ for Re_{820} [Fig. 5(i)]. A dependence on Reynolds number is nevertheless appreciable by observing that, at the same distance from the source, a higher Reynolds number corresponds to higher $\overline{u'u'}/\overline{w_c^2}$ values.

IV. INTEGRAL ANALYSIS

In this section we move to the description of radial integrated flow statistics. Our aims are to (i) characterize the vertical variation of the integral quantities in transitional, non-Boussinesq plumes; (ii) present an estimate for the local characteristic density, ρ_m ; and (iii) evaluate the vertical

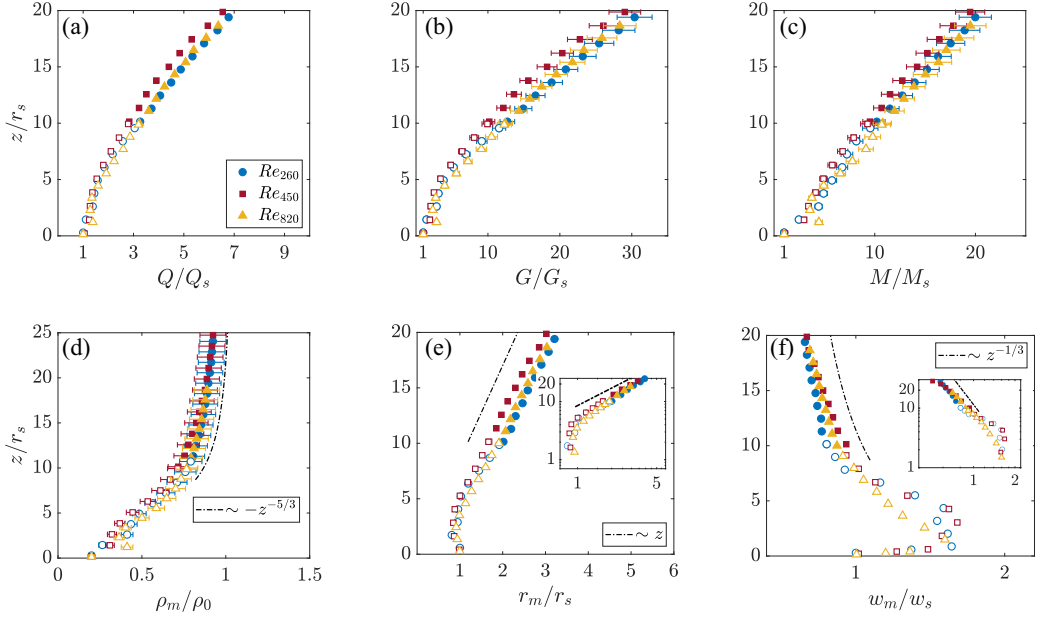


FIG. 6. (a)–(c) Vertical variation of the integral volume, mass, and momentum fluxes. (d)–(f) Characteristic density ρ_m , radius r_m , and velocity w_m . The dot-dashed lines show the power-law scaling predicted by Morton *et al.* [1].

behavior of the entrainment coefficient and the relevance of the different terms of the entrainment decomposition.

A. Integral fluxes, characteristic scales, and entrainment from volume conservation

As can be shown by manipulating the enthalpy balance equation [44], volume conservation is fully consistent with the dynamics of low-Mach non-Boussinesq releases, despite the large density differences characterizing the flow. Therefore, the combination of volume and mass balances implies the conservation of the vertical integral flux of density deficiency, $D \equiv 2 \int_0^\infty (\rho_0 - \bar{\rho}) \bar{w} r dr = D_s$ [44]. This allows us to estimate the vertical variation of the characteristic density of the plume ρ_m , without relying on any direct measurements of density or helium concentration. By writing the density deficiency as $D_s = \theta_m (\rho_0 - \rho_m) Q$, where $Q \equiv 2 \int_0^\infty \bar{w} r dr$ is the integral volume flux and θ_m is a profile coefficient (see Sec. IV B), considered equal to unity at this stage [44], we can obtain the characteristic plume density as

$$\rho_m = \rho_0 - \frac{D_s}{\theta_m Q}. \quad (6)$$

By integrating the mean vertical velocity profiles and by locally approximating the density radial profiles with top-hat profiles, it is possible to estimate the plume mass flux, G , and momentum, M :

$$G \equiv 2 \int_0^\infty \bar{\rho} \bar{w} r dr \simeq \rho_m Q, \quad M \equiv 2 \int_0^\infty \bar{\rho} \bar{w}^2 r dr \simeq 2 \rho_m \int_0^\infty \bar{w}^2 r dr = \rho_m M^*, \quad (7)$$

where the symbol $M^* \equiv 2 \int_0^\infty \bar{w}^2 r dr$ represents the specific momentum [45]. Figures 6(a)–6(c) show the resulting integral quantities: Q , G , and M . The fluxes can be exploited to obtain the plume

top-hat velocity, w_m , and radius, r_m ([15]):

$$w_m \equiv \frac{M}{G} \simeq \frac{M^*}{Q}, \quad r_m \equiv \left(\frac{QG}{M} \right)^{1/2} \simeq \frac{Q}{M^{*1/2}}. \quad (8)$$

The resulting top-hat quantities, i.e., ρ_m/ρ_0 , w_m , and r_m are presented in Figs. 6(d)–6(f). The vertical variation of the density ratio [Fig. 6(d)] shows how the turbulent entrainment causes an increase in the plume density while moving away from the source. For $z > 22r_s$, ρ_m/ρ_0 reaches 0.9, i.e., the plumes attain a Boussinesq condition. The growth of the density ratio is more intense in the near-source region, but, immediately downstream from the turbulent transition, ρ_m/ρ_0 is still close to 0.7, enabling the investigation of non-Boussinesq effects even in the turbulent zone.

Figure 6(e) shows that, before exhibiting linear spreading, the characteristic radius does not increase until $z = 4r_s$ in the three different experiments. The plume necking is concurrent with an augmentation of the characteristic velocity up to $1.8w_s$ [Fig. 6(f)], consistently with the increasing of the centerline vertical velocity [Fig. 4(a)]. This peculiar behavior is corroborated by dimensional analysis. In the region where the characteristic velocity increases, i.e., $z < r_s$, the plume radius is constant and equal to r_s . Therefore, w_m is only a function of an equivalent buoyancy flux per unit area, $D_s g / (\rho_0 \pi r_s^2)$, and of the distance from the source, z . It can be written as

$$w_m \sim \left(\frac{D_s g}{\rho_0 r_s^2} \right)^a z^b. \quad (9)$$

The concordance of measurement units is achieved for $a = b = 1/3$, justifying the plume acceleration in the z direction. Necking and acceleration in non-Boussinesq plumes are also predicted, for example, by the Fanelop and Webber [46] model, generalizing the Morton *et al.* [1] approach for plumes with density ratio significantly smaller than 1 and for non-power-law solutions. The power-law behavior of the characteristic scales predicted by the scaling argument for Boussinesq releases (black dashed line in Fig 6, [1]) is instead fairly well respected for $z > 12r_s$: within the turbulent region, the low-density ratio has negligible influence on the plume scales.

When dealing with Boussinesq releases, the mixing with ambient air is usually quantified by the coefficient α , arising from the integral volume (or mass) conservation:

$$\frac{dQ}{dz} = -2[ru]_\infty \quad (10)$$

when introducing the entrainment hypothesis $-[ru]_\infty = \alpha M^{*1/2}$ [27]. Given the volume conservation, and based on the recent experimental evidence by Salizzoni *et al.* [15], this approach can be conveniently adopted also when dealing with non-Boussinesq releases. Relying on these findings, we therefore estimate α as

$$\alpha = \frac{1}{2M^{*1/2}} \frac{dQ}{dz}. \quad (11)$$

The values of α for increasing distance from the source and for the three plumes are shown in Fig. 7(a). Despite some noise due to the numerical estimate of the vertical derivative of the volume flux Q from experimental data, the three cases show the same trend. The entrainment is close to zero at the source; it strongly increases for $0 < z < 8r_s$ and then more gradually. The α profiles are not exactly monotonic as they show a local maximum for $5r_s < z < 10r_s$. The position of the local maximum approaches the source if Re_s increases. In the upper part of the domain, α loses its dependence on Re_s and exceeds 0.1.

In Fig. 7(b), the plume variables are exploited to compute Γ , as defined in Eq. (1). In our experiments with an imposed $\Gamma = 1$ at the source, the acceleration near the source [see Fig. 4(b)] causes an increase in the inertial forcing that produces a “momentum-dominated” region (i.e., with $\Gamma < 1$). Once reaching a minimum $\Gamma \approx 0.25$, the flow tends to regain the pure plume condition in the upper part of the domain. The vertical height at which the minimum Γ occurs decreases for increasing Re_s but the qualitative behavior is the same for the three plumes.

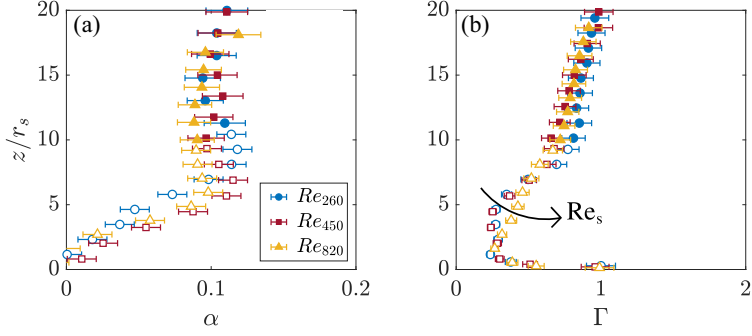


FIG. 7. (a) Entrainment obtained from volume conservation, α , and (b) plume scaled Richardson number, Γ .

B. Entrainment relation

In this section, we present a second estimate of the entrainment coefficient, obtained by combining the mass, momentum, and mean kinetic energy balance equations. This approach, referred to as entrainment decomposition, was employed primarily for investigating Boussinesq releases [16,18,28,29,47] and, only recently, low-density jets [15] and is here applied to non-Boussinesq plumes. The detailed derivation of this entrainment relation for moderate Reynolds, non-Boussinesq plumes, is presented in the Appendix. Starting from the complete relation and considering (i) that the Reynolds-averaged velocity statistics are equal to the Favre-averaged velocity statistics, (ii) a top-hat profile for the time-averaged density $\bar{\rho}(r, z)$, i.e., $\bar{\rho}(r, z) = \rho_m(z)$, and (iii) only the contribution of the mean and viscous profile coefficients [6,15,18,44], denoted with subscripts “ m ” and “ μ ” (Appendix), we obtain that the entrainment relation can be written as

$$\alpha_{E\mu} = -\frac{\rho_m}{\rho_0} \frac{\delta_m + \delta_\mu}{2(\gamma_m + \gamma_\mu)} + \frac{\rho_m}{\rho_0} r_m \frac{d}{dz} \left(\ln \frac{(\gamma_m + \gamma_\mu)^{1/2}}{1 + \beta_\mu} \right) + \left(\frac{1}{1 + \beta_\mu} - \frac{\theta_m}{\gamma_m + \gamma_\mu} \right) \text{Ri}, \quad (12)$$

where

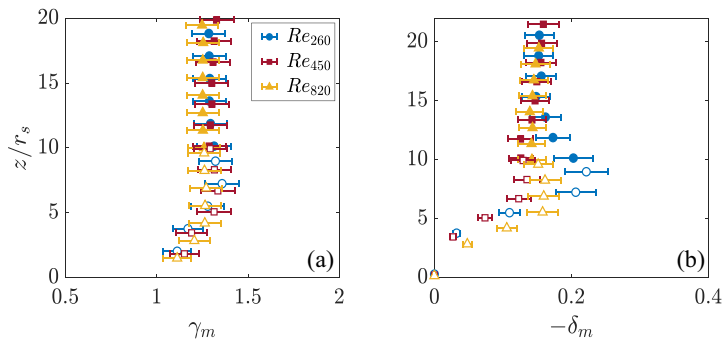
$$\gamma_m \equiv \frac{2}{w_m^3 r_m^2} \int_0^\infty \bar{w}^3 r dr, \quad \delta_m \equiv \frac{4}{w_m^3 r_m} \int_0^\infty \frac{\bar{w} d\bar{w}}{dr} r dr, \quad (13)$$

and where the terms β_μ , γ_μ , and δ_μ arise when considering the viscous terms within the balance equations. Their formulation is

$$\beta_\mu \equiv \frac{-2r_m}{\text{Re}_m} \frac{d(\ln Q)}{dz}, \quad \gamma_\mu \equiv \frac{-2}{\text{Re}_m w_m^2 r_m} \frac{dM^*}{dz}, \quad \delta_\mu \equiv \frac{-8}{w_m^2 \text{Re}_m} \int_0^\infty \left[\left(\frac{\partial \bar{w}}{\partial r} \right)^2 + \left(\frac{\partial \bar{w}}{\partial z} \right)^2 \right] r dr. \quad (14)$$

In the Re_m definition, a characteristic kinematic viscosity ν_m , obtained by weighing the helium and air viscosities according to their concentration in the plume, inferred from ρ_m , is considered. Despite the moderate Reynolds number at the source, we observe that, in the whole domain and for all three plumes, $\beta_\mu \ll 1$, $\gamma_\mu \ll \gamma_m$, and $\delta_\mu \ll \delta_m$, so that the contribution of the viscous terms is fully negligible. Therefore, the entrainment relation reduces to

$$\alpha_E = \underbrace{-\frac{\rho_m}{\rho_0} \frac{\delta_m}{2\gamma_m}}_{\alpha_{\text{prod}}} + \underbrace{\frac{\rho_m}{\rho_0} r_m \frac{d}{dz} (\ln \gamma_m^{1/2})}_{\alpha_{\text{shape}}} + \underbrace{\left(1 - \frac{\theta_m}{\gamma_m} \right)}_{\alpha_{\text{Ri}}} \text{Ri}. \quad (15)$$


 FIG. 8. Vertical variations of (a) γ_m and (b) $-\delta_m$.

A remark is necessary for the value of θ_m , which cannot be obtained relying on velocity measurements. Assuming that the profiles have a Gaussian shape, θ_m can be written as [29]

$$\theta_m = \frac{2}{\varphi^2 + 1}, \quad (16)$$

where $\varphi = \hat{r}_b/\hat{r}_m$ is the ratio between the standard deviation of the Gaussian density deficiency profile, \hat{r}_b , and the standard deviation of the Gaussian velocity profile, \hat{r}_m . The literature values of φ for Boussinesq jets and plumes show a relevant scatter. Despite this, there is a general agreement in assuming their dependence on the local value of Γ [8,29,33]. Assuming its independence on the density ratio and Reynolds number, Wang and Law [8] have proposed the following empirical relation between the local φ and Γ :

$$\varphi = \varphi_j - (\varphi_j - \varphi_p)\Gamma^\kappa, \quad (17)$$

where $\varphi_j = 1.23$ and $\varphi_p = 1.04$ are the reference values for pure jet and pure plume, respectively, and where $\kappa = 1.5$. We assume relation (17) to hold for our experimental plumes.

The profile coefficients with the greatest influence on the entrainment coefficient estimate are γ_m and δ_m , which correspond to the nondimensional flux of the mean kinetic energy and the production of turbulent kinetic energy. Their vertical profiles are presented in Figs. 8(a) and 8(b). The γ_m coefficients [Fig. 8(a)] increase in the near-source region. They attain an almost constant value at a lower vertical distance from the source for increasing Re_s . The value in the turbulent region is constant ($\gamma_m \sim 1.3$, close to $\gamma_m = 4/3$, typical for a Gaussian radial velocity profile [6]), indicating the self-similarity of the mean vertical velocity field. The $-\delta_m$ coefficients [Fig. 8(b)] show an analogous trend to γ_m with two relevant differences: (i) Re_{260} shows an overshoot at $z = 8r_s$ in correspondence with the turbulence triggering; and (ii) in the turbulent region, the influence of the Reynolds number at the source is still present, and fades out for $z > 15r_s$.

The entrainment coefficient, α_E , is obtained summing the three contributions α_{prod} , α_{Ri} , and α_{shape} . The α_{prod} term [Fig. 9(a)] is related to the rate of production of turbulent kinetic energy over the mean kinetic energy flux. It is zero at the source and has a strong increase when $z < 10r_s$, in correspondence with the turbulent transition. The growth continues in the turbulent region and, for the three plumes, $\alpha_{\text{prod}} \approx 0.55$ at $z = 20r_s$. We expect α_{prod} to increase up to 0.7 in the far field [6]. The α_{Ri} term, related to buoyancy effects and depending linearly on the Richardson number, is mainly responsible for the increased entrainment in plumes with respect to jets. As shown by Fig. 9(b), regardless of the Reynolds number at the source, α_{Ri} keeps increasing, also in the turbulent region, and exceeds 0.05 for $z > 15r_s$. The α_{shape} contribution [Fig. 9(c)] is related to the shape

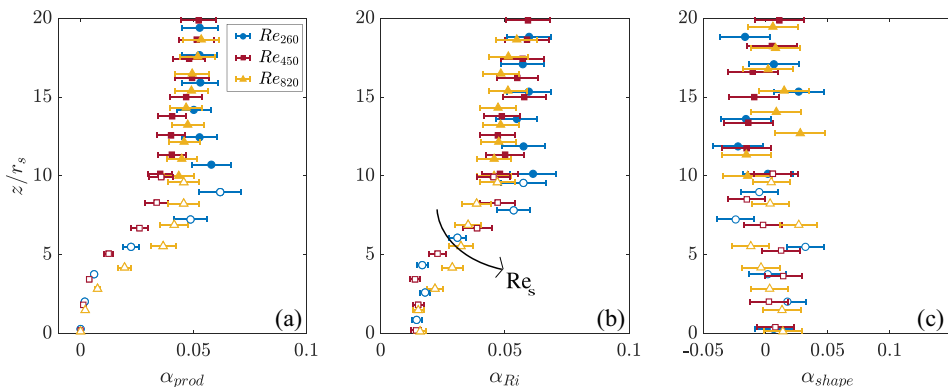


FIG. 9. Axial variation of the entrainment relation components: α_{prod} (a), α_{Ri} (b), and α_{shape} (c) for the three experimental plumes.

variation of the radial profiles for increasing distances from the source. It is identically zero in a fully self-similar condition. Above $z = 5r_s$, α_{shape} becomes negligible compared to α_{prod} and α_{Ri} .

Figure 10 shows a comparison between the two estimates of the entrainment coefficient, obtained from Eqs. (11) and (15). Note that the entrainment coefficient obtained from volume conservation [Eq. (11)] is fully independent of the one obtained from the entrainment relation Eq. (12). To satisfy volume, mass, momentum, and kinetic energy balances, the two coefficients have to match in the whole domain. Figure 10 shows that even the simplified entrainment relation provided by Eq. (15) is in good agreement with the estimate of α derived from volume conservation. Almost everywhere, and notably for $z > 4r_s$, the width of the error bars caused by the propagation of the errors on the velocity statistics is lower than the discrepancy between the two estimates. This confirms that, at first order, the errors introduced by the hypothesis considered to write Eq. (15) have a minor relevance on the entrainment coefficient estimate in non-Boussinesq plumes.

V. DISCUSSION

Finally, we aim at investigating the general dependence provided by Eq. (5), i.e., to which extent the entrainment coefficient depends on the local density ratio and on the local Richardson and Reynolds numbers. We focus on the turbulent region of the flow, i.e., where $z > 10r_s$. In this

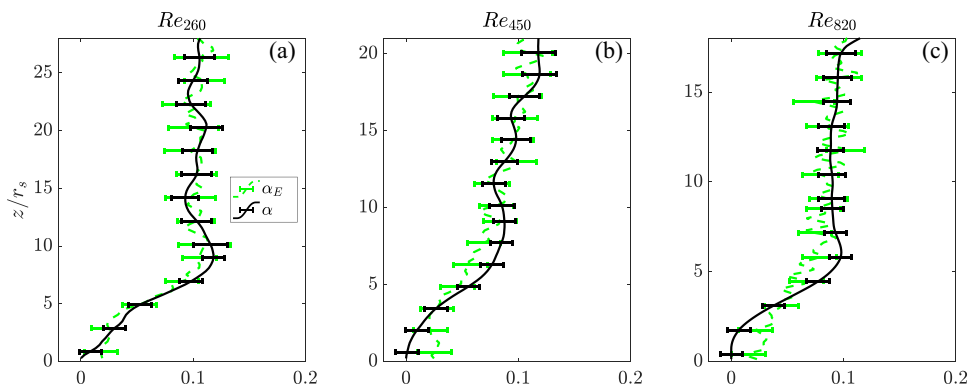


FIG. 10. Entrainment comparison for the three experimental plumes Re_{260} (a), Re_{450} (b), and Re_{820} (c). α_E is obtained from Eq. (15) and α from Eq. (11).

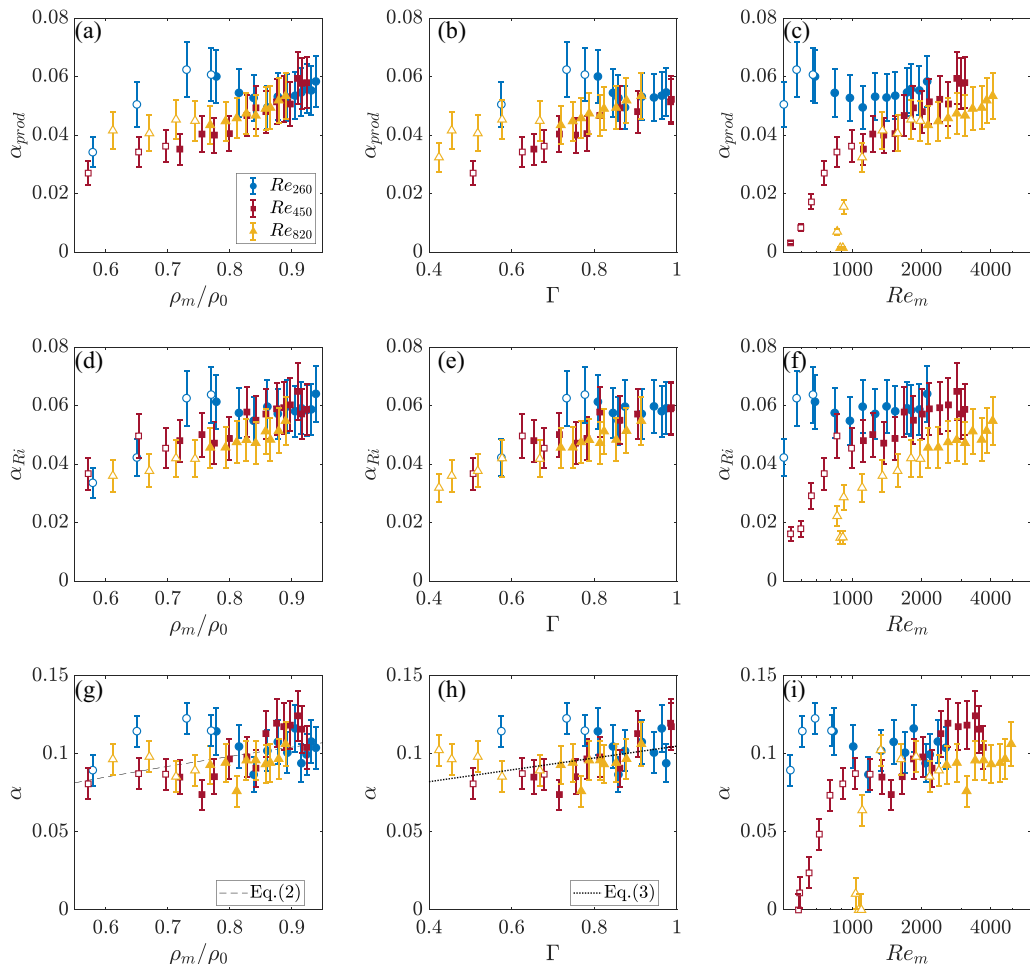


FIG. 11. Measured α_{prod} , α_{Ri} , and α as a function of the local density ratio ρ_m/ρ_0 [(a),(d),(g)], Richardson number Γ [(b),(e),(h)], and Reynolds number Re_m [(c),(f),(i)] for the three experimental plumes. The hollow symbols refer to the $z < 10r_s$ region.

region, the density ratio [Fig. 6(d)], Γ [Fig. 7(b)], and Re_m increase. In order to understand how these parameters influence the physical mechanisms of the entrainment, we initially consider the behavior of the two most significant terms of the entrainment decomposition in the turbulent zone: α_{prod} [Figs. 11(a)–11(c)] and α_{Ri} [Figs. 11(d)–11(f)].

The α_{prod} coefficient exhibits, even in the turbulent region, a dependence on the Reynolds number at the source that is canceled only for $\rho_m/\rho_0 > 0.8$ and $\Gamma > 0.8$ (corresponding to a height of $z > 15r_s$). For Re_{450} and Re_{820} , a monotonic increase in α_{prod} is observed, concurrently with the increase of ρ_m/ρ_0 , Γ , and Re_m . However, the vertical profiles of α_{prod} obtained here are analogous to those observed in high Reynolds iso- and variable-density jets, and Boussinesq forced plumes (i.e., they have a null value at the source that increases in the first tens of source radii) [15,18]. Salizzoni *et al.* [15] have recently shown (verifying that the α_{prod} vertical profiles in an isodensity jet and in a jet with a density ratio significantly smaller than 1 at the source are almost coincident) that the increase of α_{prod} up to $z = 30r_s$ does not exhibit a dependence on the density ratio, but is rather the product of a rising turbulent kinetic energy production, while moving away from the

source, due to the development of the flow in the near-source region, and occurring independently of the local density values. Arguably, the same reasoning can be applied to buoyant releases.

Concerning α_{Ri} , Figs. 11(d) and 11(e) show its increasing trend with respect to both ρ_m/ρ_0 and Γ . Given the definition of α_{Ri} [Eq. (15)], its increase can be fully attributed to Γ . Indeed, the other parameters affecting the value of α_{Ri} are γ_m , which is constant in the turbulent region, and θ_m , which depends on Γ , only. We can therefore discard any eventual influence of ρ_m/ρ_0 on α_{Ri} . In our experimental plumes, the increase of Γ with the distance from the source z is concurrent with the increase of the density ratio due to the mixing of the plume with the ambient fluid. This justifies the observed increasing trend of α_{Ri} with the density ratio.

Figures 11(g)–11(i) report the plots of the entrainment coefficient α as a function of ρ_m/ρ_{amb} , Γ , and Re_m , respectively. For $z > 10r_s$, the experimental values of α as a function of the density ratio show a trend in agreement with the scaling predicted by Eq. (2) [black-dashed line in Fig. 11(g)]. However, considering the discussion on the α_{prod} and α_{Ri} coefficients, the increase of α with z (and therefore with ρ_m/ρ_0) is primarily associated with (i) the vertical development of the turbulence dynamics (that occurs similarly in Boussinesq and non-Boussinesq releases) and (ii) the increasing of Γ . The growth of the density ratio is not the predominant cause of the enhanced mixing for increasing distances from the source. Figure 11(h) shows that the trend of the entrainment coefficient is fairly linear with Γ , as predicted by Eq. (3) (black-dotted line) for self-similar (i.e., $\alpha_{\text{shape}} = 0$) Boussinesq releases assuming a constant α_{prod} [16,17]. This explains why our results follow Eq. (3) especially for $\Gamma > 0.8$ (i.e., $z > 15r_s$), where variations in α_{prod} are less significant.

VI. CONCLUSIONS

An experimental study on transitional, helium plumes with $\Gamma = 1$ at the source has been carried out performing PIV measurements. The aim is to describe the dynamics of these releases and provide an experimental investigation of the turbulent entrainment in non-Boussinesq steady plumes. We report here our main findings:

(a) A transition from a quasilaminar, Rayleigh-Taylor instability-dominated region to a more chaotic, turbulent zone is present above the source. The transition position gets closer to the source for increasing Reynolds number at the source.

(b) The experimental plumes exhibit necking and acceleration above the source. A forced-plume region is created in correspondence to this acceleration.

(c) A methodology to derive the characteristic plume density relying on the conservation of the density deficiency flux has been proposed. The mixing with the ambient air causes an increase in the plume density. The density ratio reaches 0.9 after $22r_s$; above that height the plumes can be considered as “Boussinesq.”

(d) The α_{prod} contribution is null at the release and increases for rising distance from the source. This increment is analogous to that recently observed both in Boussinesq and non-Boussinesq releases due to the vertical development of the turbulence dynamics [15,18].

(e) Downstream from the turbulent transition, both ρ_m/ρ_0 and Γ increase with z in our experimental plumes. Given that α_{Ri} increases by definition with Γ , an increasing trend is also present when α_{Ri} is plotted against ρ_m/ρ_0 .

(f) In the turbulent flow region, the scaling predicted by Ricou and Spalding [10] aligns well with our experimental results. However, based on observations on α_{prod} and α_{Ri} , we cannot conclude that an enhanced density ratio is the physical cause of the more intense mixing process while moving away from the source.

Further experimental and numerical studies are needed to better understand the role of large density differences on the entrainment phenomenon, especially to broaden the findings presented in this study to non-Boussinesq plumes with high Reynolds numbers at the source and with variations of the density difference over more than one order of magnitude.

Supporting data for this article are available on request.

ACKNOWLEDGMENTS

We would like to thank H. Correia (LMFA) and N. Grosjean (LMFA) who contributed their laboratory expertise and S. Vaux (IRSN) for fruitful discussions.

APPENDIX: NON-BOUSSINESQ ENTRAINMENT DECOMPOSITION WITH VISCOUS TERMS

The purpose of this Appendix is to provide the complete version of the entrainment decomposition for moderate-Reynolds, non-Boussinesq plumes.

The equations are written considering Favre-averaged statistics. The Favre averages are denoted by a tilde and defined as $\tilde{\xi} = \overline{\rho\xi}/\bar{\rho}$ (so that the variance writes $\tilde{\sigma}_\xi^2 = \overline{\rho(\tilde{\xi} - \xi)^2}/\bar{\rho}$), where the overbar denotes Reynolds average.

The time-averaged conservation equations for mass and momentum (in the z direction) can be expressed as, respectively,

$$\frac{1}{r} \frac{\partial}{\partial r} r(\bar{\rho}\tilde{u}) + \frac{\partial}{\partial z} (\bar{\rho}\tilde{w}) = 0, \quad (\text{A1})$$

$$\frac{1}{r} \frac{\partial}{\partial r} r(\bar{\rho}\tilde{u}\tilde{w} + \overline{\rho u'' w''}) + \frac{\partial}{\partial z} (\bar{\rho}\tilde{w}^2 + \overline{\rho w''^2}) = -\frac{\partial \bar{p}}{\partial z} + \rho_0 \bar{b} + \mu \left[\frac{1}{r} \frac{\partial}{\partial r} \left(r \frac{\partial \bar{w}}{\partial r} \right) + \frac{\partial^2 \bar{w}}{\partial z^2} \right], \quad (\text{A2})$$

where \bar{p} is the pressure difference relative to the hydrostatic pressure p_0 (defined such that $\frac{\partial}{\partial z} p_0 = -\rho_0 g$, with g the gravitational acceleration, $\bar{b} = g(\rho_0 - \bar{\rho})/\rho_0$ is the local buoyancy, and μ is the dynamic viscosity. Multiplying (A2) by $2\tilde{w}$ and using (A1) yields

$$\begin{aligned} & \frac{1}{r} \frac{\partial}{\partial r} r \left(\bar{\rho}\tilde{u}\tilde{w}^2 + 2\overline{\rho u'' w''} \tilde{w} - 2\mu \frac{\partial \bar{w}}{\partial r} \tilde{w} \right) + \frac{\partial}{\partial z} \left(\bar{\rho}\tilde{w}^3 + 2\overline{\rho w''^2} \tilde{w} + 2\bar{p}\tilde{w} - 2\mu \frac{\partial \bar{w}}{\partial z} \tilde{w} \right) \\ & = 2\overline{\rho u'' w''} \frac{\partial}{\partial r} \tilde{w} + 2\overline{\rho w''^2} \frac{\partial}{\partial z} \tilde{w} + 2\bar{p} \frac{\partial}{\partial z} \tilde{w} + 2\rho_0 \bar{b} \tilde{w} - 2\mu \left(\frac{\partial \bar{w}}{\partial r} \frac{\partial \tilde{w}}{\partial r} + \frac{\partial \bar{w}}{\partial z} \frac{\partial \tilde{w}}{\partial z} \right). \end{aligned} \quad (\text{A3})$$

Integrating (A1), (A2), and (A3) over r (between the plume axis and infinity) we then obtain

$$\frac{d\tilde{G}}{dz} = -2\rho_0 [r\tilde{u}]_\infty, \quad (\text{A4})$$

$$\frac{d}{dz} (\tilde{\beta}_g \tilde{M}) = \rho_0 \tilde{B}, \quad (\text{A5})$$

$$\frac{d}{dz} \left(\tilde{\gamma}_g \frac{\tilde{M}^2}{\tilde{G}} \right) = \tilde{\delta}_g \frac{\tilde{M}^{5/2}}{\tilde{Q}^{1/2} \tilde{G}^{3/2}} + \rho_0 \tilde{\theta}_m \frac{\tilde{B}\tilde{M}}{\tilde{G}}, \quad (\text{A6})$$

where the mass flux, \tilde{G} , momentum flux, \tilde{M} , volume flux, \tilde{Q} , and integral buoyancy, \tilde{B} , are defined as, respectively,

$$\tilde{G} \equiv 2 \int_0^\infty \bar{\rho}\tilde{w}r \, dr, \quad \tilde{M} \equiv 2 \int_0^\infty \bar{\rho}\tilde{w}^2 r \, dr, \quad \tilde{Q} \equiv 2 \int_0^\infty \tilde{w}r \, dr, \quad \tilde{B} \equiv 2 \int_0^\infty \bar{b}r \, dr, \quad (\text{A7})$$

and where $\tilde{\beta}_g = \tilde{\beta}_m + \tilde{\beta}_f + \tilde{\beta}_p + \tilde{\beta}_\mu$, $\tilde{\gamma}_g = \tilde{\gamma}_m + \tilde{\gamma}_f + \tilde{\gamma}_p + \tilde{\gamma}_\mu$, and $\tilde{\delta}_g = \tilde{\delta}_m + \tilde{\delta}_f + \tilde{\delta}_p + \tilde{\delta}_\mu$ are profile coefficients, associated with the radial variations of the mean flow (denoted with subscript "m"), velocity fluctuations (denoted with subscript "f") or with the mean pressure (denoted with subscript "p"). The profile coefficients associated with the radial variations of the mean flow are defined as

$$\begin{aligned} \tilde{\beta}_m & \equiv \frac{2}{\tilde{\rho}_m \tilde{w}_m^2 \tilde{r}_m^2} \int_0^\infty \bar{\rho}\tilde{w}^2 r \, dr = 1, & \tilde{\theta}_m & \equiv \frac{2}{\tilde{b}_m \tilde{w}_m \tilde{r}_m^2} \int_0^\infty \bar{b}\tilde{w}r \, dr, \\ \tilde{\gamma}_m & \equiv \frac{2}{\tilde{\rho}_m \tilde{w}_m^3 \tilde{r}_m^2} \int_0^\infty \bar{\rho}\tilde{w}^3 r \, dr, & \tilde{\delta}_m & \equiv \frac{4}{\tilde{\rho}_m \tilde{w}_m^3 \tilde{r}_m} \int_0^\infty \overline{\rho w'' u''} \frac{\partial \tilde{w}}{\partial r} r \, dr, \end{aligned} \quad (\text{A8})$$

those associated with the fluctuations of the velocity or with the mean pressure are

$$\begin{aligned}\tilde{\beta}_f &\equiv \frac{2}{\tilde{\rho}_m \tilde{w}_m^2 \tilde{r}_m^2} \int_0^\infty \tilde{\rho} \tilde{w}'^2 r \, dr, & \tilde{\beta}_p &\equiv \frac{2}{\tilde{\rho}_m \tilde{w}_m^2 \tilde{r}_m^2} \int_0^\infty \tilde{p} r \, dr, \\ \tilde{\gamma}_f &\equiv \frac{4}{\tilde{\rho}_m \tilde{w}_m^3 \tilde{r}_m^2} \int_0^\infty \tilde{\rho} \tilde{w} \tilde{w}'^2 r \, dr, & \tilde{\gamma}_p &\equiv \frac{4}{\tilde{\rho}_m \tilde{w}_m^3 \tilde{r}_m^2} \int_0^\infty \tilde{w} \tilde{p} r \, dr, \\ \tilde{\delta}_f &\equiv \frac{4}{\tilde{\rho}_m \tilde{w}_m^3 \tilde{r}_m} \int_0^\infty \tilde{\rho} \tilde{w}'^2 \frac{\partial \tilde{w}}{\partial z} r \, dr, & \tilde{\delta}_p &\equiv \frac{4}{\tilde{\rho}_m \tilde{w}_m^3 \tilde{r}_m} \int_0^\infty \tilde{p} \frac{\partial \tilde{w}}{\partial z} r \, dr,\end{aligned}\quad (\text{A9})$$

and those associated with the viscous stresses are

$$\begin{aligned}\tilde{\beta}_\mu &\equiv \frac{-2\mu}{\tilde{\rho}_m \tilde{w}_m^2 \tilde{r}_m^2} \int_0^\infty \frac{\partial \tilde{w}}{\partial z} r \, dr, & \tilde{\delta}_\mu &\equiv \frac{-4\mu}{\tilde{\rho}_m \tilde{w}_m^3 \tilde{r}_m} \int_0^\infty \left(\frac{\partial \tilde{w}}{\partial r} \frac{\partial \tilde{w}}{\partial r} + \frac{\partial \tilde{w}}{\partial z} \frac{\partial \tilde{w}}{\partial z} \right) r \, dr. \\ \tilde{\gamma}_\mu &\equiv \frac{-4\mu}{\tilde{\rho}_m \tilde{w}_m^3 \tilde{r}_m^2} \int_0^\infty \tilde{w} \frac{\partial \tilde{w}}{\partial z} r \, dr,\end{aligned}\quad (\text{A10})$$

Salizzoni *et al.* [15] showed that the differences between Reynolds averaged and Favre averaged are very slight for the mean longitudinal velocity. In (A10), replacing \bar{w} by \tilde{w} gives after some simplification

$$\tilde{\beta}_\mu \equiv \frac{-2\tilde{r}_m}{\tilde{\text{Re}}_m} \frac{d(\ln \tilde{Q})}{dz}, \quad \tilde{\gamma}_\mu \equiv \frac{-2}{\tilde{\text{Re}}_m \tilde{w}_m^2 \tilde{r}_m} \frac{d\tilde{M}^*}{dz}, \quad \delta_\mu \equiv \frac{-2\tilde{\epsilon}}{\tilde{\text{Re}}_m}, \quad (\text{A11})$$

with $\tilde{M}^* = \int_0^\infty \tilde{w}^2 r \, dr$, $\tilde{\epsilon} = \frac{4}{\tilde{w}_m^2} \int_0^\infty [(\frac{\partial \tilde{w}}{\partial r})^2 + (\frac{\partial \tilde{w}}{\partial z})^2] r \, dr$ and $\tilde{\text{Re}}_m = \frac{\tilde{\rho}_m \tilde{w}_m^2 \tilde{r}_m}{\mu}$ is the z -dependent Reynolds number obtained with the Favre-averaged scales.

In these definitions, we have made use of a "top-hat" plume width \tilde{r}_m , velocity \tilde{w}_m , density $\tilde{\rho}_m$, and buoyancy \tilde{b}_m , which are consistently defined using integral quantities as [6]

$$\tilde{r}_m \equiv \frac{\tilde{Q}^{1/2} \tilde{G}^{1/2}}{\tilde{M}^{1/2}}, \quad \tilde{w}_m \equiv \frac{\tilde{M}}{\tilde{G}}, \quad \tilde{\rho}_m \equiv \frac{\tilde{G}}{\tilde{Q}}, \quad \tilde{b}_m \equiv \frac{\tilde{B}\tilde{M}}{\tilde{Q}\tilde{G}}. \quad (\text{A12})$$

By definition of the entrainment coefficient, the radial volume flux of the entrained ambient fluid in (A4) is assumed to be proportional to the longitudinal velocity of the plume:

$$\tilde{\alpha} \equiv \frac{-[r\tilde{u}]_\infty}{\tilde{r}_m \tilde{w}_m}. \quad (\text{A13})$$

Combining (A4), (A12), and (A13) the entrainment coefficient can be expressed as

$$\tilde{\alpha} = \frac{\tilde{\rho}_m \tilde{r}_m}{\rho_0} \frac{d\tilde{G}}{2\tilde{G} dz}. \quad (\text{A14})$$

Equations (A5) and (A6) in turn become

$$\frac{\tilde{\rho}_m \tilde{r}_m}{\rho_0} \frac{d}{\tilde{M}} (\tilde{\beta}_g \tilde{M}) = \tilde{\text{Ri}}, \quad (\text{A15})$$

$$\frac{\tilde{\rho}_m \tilde{r}_m \tilde{G}}{\rho_0 \tilde{M}^2} \frac{d}{dz} \left(\tilde{\gamma}_g \frac{\tilde{M}^2}{\tilde{G}} \right) = \frac{\tilde{\rho}_m}{\rho_0} \tilde{\delta}_g + 2\tilde{\theta}_m \tilde{\text{Ri}}, \quad (\text{A16})$$

where $\tilde{\text{Ri}}$ is the plume Richardson number, a parameter varying with the distance from the source, defined as

$$\tilde{\text{Ri}} \equiv \frac{\tilde{b}_m \tilde{r}_m}{\tilde{w}_m^2} = \frac{\tilde{G} \tilde{B}}{\tilde{Q} \tilde{M}} \left(\frac{\tilde{Q}\tilde{G}}{\tilde{M}} \right)^{1/2}, \quad (\text{A17})$$

so that $\tilde{Ri}(z=0) = \tilde{Ri}_s$.

Finally, by rearranging (A15) and (A16), we can retrieve the complete formulation for the entrainment coefficient:

$$\tilde{\alpha}_E = \underbrace{-\frac{\tilde{\rho}_m}{\rho_0} \frac{\tilde{\delta}_g}{2\tilde{\gamma}_g}}_{\tilde{\alpha}_{\text{prod}}} + \underbrace{\frac{\tilde{\rho}_m \tilde{r}_m}{\rho_0} \frac{d}{dz} \left(\ln \frac{\tilde{\gamma}_g^{1/2}}{\tilde{\beta}_g} \right)}_{\tilde{\alpha}_{\text{shape}}} + \underbrace{\left(\frac{1}{\tilde{\beta}_g} - \frac{\tilde{\theta}_m}{\tilde{\gamma}_g} \right)}_{\tilde{\alpha}_{\text{Ri}}} \tilde{Ri}. \quad (\text{A18})$$

-
- [1] B. R. Morton, G. I. Taylor, and J. S. Turner, Turbulent gravitational convection from maintained and instantaneous sources, *Proc. R. Soc. London, Ser. A* **234**, 1 (1956).
- [2] E. J. List, Turbulent jets and plumes, *Annu. Rev. Fluid Mech.* **14**, 189 (1982).
- [3] N. B. Kaye, Turbulent plumes in stratified environments: A review of recent work, *Atmos.-Ocean* **46**, 433 (2008).
- [4] A. W. Woods, Turbulent plumes in nature, *Annu. Rev. Fluid Mech.* **42**, 391 (2010).
- [5] A. Ezzamel, P. Salizzoni, and G. Hunt, Dynamical variability of axisymmetric buoyant plumes, *J. Fluid Mech.* **765**, 576 (2015).
- [6] M. van Reeuwijk and J. Craske, Energy-consistent entrainment relations for jets and plumes, *J. Fluid Mech.* **782**, 333 (2015).
- [7] G. R. Hunt and N. B. Kaye, Lazy plumes, *J. Fluid Mech.* **533**, 329 (2005).
- [8] H. Wang and A. Law, Second-order integral model for a round turbulent buoyant jet, *J. Fluid Mech.* **459**, 397 (2002).
- [9] G. K. Batchelor, Heat convection and buoyancy effects in fluids, *Q. J. R. Meteorol. Soc.* **80**, 339 (1954).
- [10] F. P. Ricou and D. B. Spalding, Measurements of entrainment by axisymmetrical turbulent jets, *J. Fluid Mech.* **11**, 21 (1961).
- [11] P. Crapper and W. Baines, Non Boussinesq forced plumes, *Atmos. Environ.* **11**, 415 (1977).
- [12] P. Crapper and W. Baines, Some remarks on non-boussinesq forced plumes, *Atmos. Environ.* **12**, 1939 (1978).
- [13] A. W. Woods, A note on non-boussinesq plumes in an incompressible stratified environment, *J. Fluid Mech.* **345**, 347 (1997).
- [14] T. S. Van Den Bremer and G. R. Hunt, Universal solutions for boussinesq and non-boussinesq plumes, *J. Fluid Mech.* **644**, 165 (2010).
- [15] P. Salizzoni, S. Vaux, M. Creyssels, M. Amielh, L. Pietri, and F. Anselmet, Turbulent transfer and entrainment in a low-density jet, *J. Fluid Mech.* **968**, A27 (2023).
- [16] C. H. B. Priestley and F. K. Ball, Continuous convection from an isolated source of heat, *Q. J. R. Meteorol. Soc.* **81**, 144 (1955).
- [17] E. J. List and J. Imberger, Turbulent entrainment in buoyant jets and plumes, *J. Hydraulics Division* **99**, 1461 (1973).
- [18] M. van Reeuwijk, P. Salizzoni, G. R. Hunt, and J. Craske, Turbulent transport and entrainment in jets and plumes: A DNSstudy, *Phys. Rev. Fluids* **1**, 074301 (2016).
- [19] G. Heskestad, Dynamics of the fire plume, *Philos. Trans. R. Soc. London, Ser. A* **356**, 2815 (1998).
- [20] G. Heskestad, Fire plumes, flame height, and air entrainment, in *SFPE Handbook of Fire Protection Engineering*, edited by M. J. Hurley, D. Gottuk, J. R. Hall, K. Harada, E. Kuligowski, M. Puchovsky, J. Torero, J. M. Watts, and C. Wieczorek (Springer, New York, 2016), pp. 396–428.
- [21] B. Viggiano, T. Dib, N. Ali, L. G. Mastin, R. B. Cal, and S. A. Solovitz, Turbulence, entrainment and low-order description of a transitional variable-density jet, *J. Fluid Mech.* **836**, 1009 (2018).
- [22] A. Shabbir and W. K. George, Experiments on a round turbulent buoyant plume, *J. Fluid Mech.* **275**, 1 (1994).

- [23] W. K. George, Jr., R. L. Alpert, and F. Tamanini, Turbulence measurements in an axisymmetric buoyant plume, *Int. J. Heat Mass Transfer* **20**, 1145 (1977).
- [24] H. Petersen, The properties of helium: Density, specific heats, viscosity, and thermal conductivity at pressures from 1 to 100 bar and from room temperature to about 1800 K, Risoe-R No. 224 (Risø National Laboratory, 1970).
- [25] M. A. Meehan, N. T. Wimer, and P. E. Hamlington, Richardson and Reynolds number effects on the near field of buoyant plumes: Temporal variability and puffing, *J. Fluid Mech.* **950**, A24 (2022).
- [26] T. J. O'Hern, E. J. Weckman, A. L. Gerhart, S. R. Tieszen, and R. W. Schefer, Experimental study of a turbulent buoyant helium plume, *J. Fluid Mech.* **544**, 143 (2005).
- [27] J. S. Turner, Turbulent entrainment: The development of the entrainment assumption, and its application to geophysical flows, *J. Fluid Mech.* **173**, 431 (1986).
- [28] E. Kaminski, S. Tait, and G. Carazzo, Turbulent entrainment in jets with arbitrary buoyancy, *J. Fluid Mech.* **526**, 361 (2005).
- [29] J. Craske, P. Salizzoni, and M. van Reeuwijk, The turbulent Prandtl number in a pure plume is $3/5$, *J. Fluid Mech.* **822**, 774 (2017).
- [30] L. Milton-McGurk, N. Williamson, S. Armfield, M. Kirkpatrick, and K. Talluru, Entrainment and structure of negatively buoyant jets, *J. Fluid Mech.* **911**, A21 (2021).
- [31] L. Milton-McGurk, N. Williamson, S. Armfield, and M. Kirkpatrick, Characterising entrainment in fountains and negatively buoyant jets, *J. Fluid Mech.* **939**, A29 (2022).
- [32] J. S. Salinas, S. Zúñiga, M. Cantero, M. Shringarpure, J. Fedele, D. Hoyal, and S. Balachandar, Slope dependence of self-similar structure and entrainment in gravity currents, *J. Fluid Mech.* **934**, R4 (2022).
- [33] P. N. Papanicolaou and E. J. List, Investigations of round vertical turbulent buoyant jets, *J. Fluid Mech.* **195**, 341 (1988).
- [34] A. Sciacchitano and B. Wieneke, PIV uncertainty propagation, *Meas. Sci. Technol.* **27**, 084006 (2016).
- [35] L. Milton-McGurk, N. Williamson, S. Armfield, and M. Kirkpatrick, Experimental investigation into turbulent negatively buoyant jets using combined PIV and PLIF measurements, *Int. J. Heat Fluid Flow* **82**, 108561 (2020).
- [36] L. H. Benedict and R. D. Gould, Towards better uncertainty estimates for turbulence statistics, *Exp. Fluids* **22**, 129 (1996).
- [37] P. Huerre and P. A. Monkewitz, Local and global instabilities in spatially developing flows, *Annu. Rev. Fluid Mech.* **22**, 473 (1990).
- [38] D. M. Kyle and K. R. Sreenivasan, The instability and breakdown of a round variable-density jet, *J. Fluid Mech.* **249**, 619 (1993).
- [39] P. A. Monkewitz, D. W. Bechert, B. Barsikow, and B. Lehmann, Self-excited oscillations and mixing in a heated round jet, *J. Fluid Mech.* **213**, 611 (1990).
- [40] B. M. Cetegen and T. A. Ahmed, Experiments on the periodic instability of buoyant plumes and pool fires, *Combust. Flame* **93**, 157 (1993).
- [41] B. M. Cetegen and K. D. Kasper, Experiments on the oscillatory behavior of buoyant plumes of helium and helium-air mixtures, *Phys. Fluids* **8**, 2974 (1996).
- [42] B. M. Cetegen, Measurements of instantaneous velocity field of a non-reacting pulsating buoyant plume by particle image velocimetry, *Combust. Sci. Technol.* **123**, 377 (1997).
- [43] H. J. Hussein, S. P. Capp, and W. K. George, Velocity measurements in a high-Reynolds-number, momentum-conserving, axisymmetric, turbulent jet, *J. Fluid Mech.* **258**, 31 (1994).
- [44] G. G. Rooney and P. F. Linden, Similarity considerations for non-Boussinesq plumes in an unstratified environment, *J. Fluid Mech.* **318**, 237 (1996).
- [45] G. R. Hunt and N. G. Kaye, Virtual origin correction for lazy turbulent plumes, *J. Fluid Mech.* **435**, 377 (2001).
- [46] T. K. Fannelop and D. M. Webber, On buoyant plumes rising from area sources in a calm environment, *J. Fluid Mech.* **497**, 319 (2003).
- [47] A. Ezzamel, Free and confined buoyant flows, Ph.D. thesis, Imperial College London, UK, 2011.